A Genuinely Multi-Dimensional Upwind Cell-Vertex Scheme for the Euler Equations

Kenneth G. Powell and Bram van Leer
The University of Michigan
Ann Arbor, Michigan

and *Institute for Computational Mechanics in Propulsion*
Lewis Research Center
Cleveland, Ohio

May 1989

NASA

ICOMP

A Genuinely Multi-Dimensional Upwind Cell-Vertex Scheme for the Euler Equations

Kenneth G. Powell[*] and Bram van Leer[*]
Department of Aerospace Engineering
The University of Michigan, Ann Arbor, Michigan 48109

and Institute for Computational Mechanics in Propulsion
Lewis Research Center, Cleveland, Ohio 44135

Abstract

A scheme for solving the two-dimensional Euler equations is developed. It is based on a new scheme for the two-dimensional linear convection equation, and the Euler-equation decomposition developed by Hirsch et al. [1]. The scheme is genuinely two-dimensional. At each iteration, the data are locally decomposed into four variables, allowing convection in appropriate directions. This is done via a cell-vertex scheme with a downwind-weighted distribution step. The scheme is conservative, and third-order accurate in space. The derivation and stability analysis of the scheme for the convection equation, and the derivation of the extension to the Euler equations are given. Preconditioning techniques based on local values of the convection speeds are discussed. The scheme for the Euler equations is applied to two channel-flow problems. It is shown to converge rapidly to a solution that agrees well with that of a third-order upwind solver.

Introduction

Much of the understanding of modern upwind schemes for the Euler equations has come from designing algorithms for the one-dimensional linear convection equation

$$\frac{\partial u}{\partial t} + c \frac{\partial u}{\partial x} = 0.$$

As a consequence of this, problems in two or three dimensions are typically solved in a direction-split manner, with the upwinding directions normal to the faces of the computational cell. This leads to schemes that are strongly coupled to the grid on which they are applied. Discontinuities that lie along grid lines are represented properly when treated in this manner, but ones that are oblique to the grid are interpreted incorrectly by the built-in "Riemann solver" [2]. This suggests the need for designing an upwind-differencing scheme for the Euler equations that is truly multi-dimensional, and therefore less strongly coupled to the grid. The design

of an algorithm of this type should be motivated by the two-dimensional linear convection equation

$$\frac{\partial u}{\partial t} + c_x \frac{\partial u}{\partial x} + c_y \frac{\partial u}{\partial y} = 0,$$

and by an understanding of the wave-like character of the two-dimensional Euler equations.

Characteristic information has been used in the past to formulate schemes. Moretti's λ-scheme [3] and the QAZ1D algorithm of Verhoff and O'Neil [4] are two examples of non-conservative, characteristic-based schemes that use grid-decoupled stencils. Conservative schemes that are decoupled from the grid are more rare, however. Davis [5] has formulated an upwind scheme in which the Riemann problem is not solved normal to cell faces, but normal to shock waves. Levy et al. [6] have extended this work, including other possible upwinding directions. Hirsch et al. [1] have developed a method of decomposing the Euler equations into a set of convection equations. They have formulated a first-order scheme based on this decomposition. Roe [2] has developed a different decomposition method, based on locally decomposing the data into waves. He has formulated a first-order scheme that makes use of his decomposition. All of these conservative algorithms are extremely nonlinear. Differences are not taken in grid-contravariant directions, but in directions determined by local values of the flow variables. In general, the directions are actually based on *derivatives* of flow quantities. For this reason, these schemes are inherently less robust than schemes that use the grid-contravariant directions.

Most of the upwind schemes used to date are cell-centered schemes. While cell-vertex schemes have advantages in terms of accuracy [7], the ones that have been developed for the Euler equations thus far are based on central differencing [8,9] or on the Lax-Wendroff scheme [10,11]. In the central-differencing version of a cell-vertex scheme, the residual for the cell is distributed equally to the four nodes of the cell. In the Lax-Wendroff version, this distribution is altered by the higher-order terms, so that the nodes receive unequal portions of the residual. This can be generalized so that the nodes receive some weighted fraction

1

of the residual, where the weight is determined from the stability analysis of the scheme. For a convection problem, the weights should be such that the residual is "pushed" downwind. For the Euler equations, there is the added difficulty of determining what variables should be convected, and in what directions.

For the design of a genuinely multi-dimensional upwind cell-vertex scheme, then, the following components are necessary:

1. a cell-vertex scheme with a downwind-biased distribution for a scalar convection equation in which the grid components of the convection speed are known;

2. a method of locally decomposing the Euler equations into a set of convection equations;

3. an extension of the scalar scheme to a system, such that mass, momentum and energy are conserved.

These components are described below for the case of two-dimensions.

Scheme for the Convection Equation

The heart of the new scheme for the Euler equations is a cell-vertex scheme for a two-dimensional convection equation

$$\frac{\partial u}{\partial t} = -c_x \frac{\partial u}{\partial x} - c_y \frac{\partial u}{\partial y} . \tag{1}$$

This scheme is analyzed below. On a uniform Cartesian grid, the residual for the convection equation is given by

$$
\begin{aligned}
Res_{i+\frac{1}{2},j+\frac{1}{2}} &= -\frac{c_x}{\Delta x} \left(u_{i+1,j+\frac{1}{2}} - u_{i,j+\frac{1}{2}} \right) \\
&- \frac{c_y}{\Delta y} \left(u_{i+\frac{1}{2},j+1} - u_{i+\frac{1}{2},j} \right) , \tag{2}
\end{aligned}
$$

where the semi-integer index denotes a average over a cell-face, i.e.

$$u_{i+\frac{1}{2},j} = \frac{1}{\Delta x} \int_{x_i}^{x_{i+1}} u_j(x)\, dx$$

$$u_{i,j+\frac{1}{2}} = \frac{1}{\Delta y} \int_{y_j}^{y_{j+1}} u_i(y)\, dy .$$

These cell-face averages, to fourth order, may be written as

$$u_{i+\frac{1}{2},j} = \frac{u_{i,j} + u_{i+1,j}}{2} - \frac{\Delta x^2}{12} \left(\frac{\partial^2 u}{\partial x^2} \right)_{i+\frac{1}{2},j}$$

$$u_{i,j+\frac{1}{2}} = \frac{u_{i,j} + u_{i,j+1}}{2} - \frac{\Delta x^2}{12} \left(\frac{\partial^2 u}{\partial y^2} \right)_{i,j+\frac{1}{2}} ,$$

and are approximated here by the third-order accurate one-parameter formulas

$$
\begin{aligned}
u_{i+\frac{1}{2},j} &= \frac{u_{i,j} + u_{i+1,j}}{2} \\
&- \frac{\delta_x^2}{24} \left\{ (1 + \theta_x)\, u_{i+1,j} + (1 - \theta_x)\, u_{i,j} \right\} \tag{3}
\end{aligned}
$$

$$
\begin{aligned}
u_{i,j+\frac{1}{2}} &= \frac{u_{i,j} + u_{i,j+1}}{2} \\
&- \frac{\delta_y^2}{24} \left\{ (1 + \theta_y)\, u_{i,j+1} + (1 - \theta_y)\, u_{i,j} \right\} , \tag{4}
\end{aligned}
$$

where δ_x^2 and δ_y^2 are the centered second-difference operators

$$\delta_x^2 u_{i,j} = u_{i+1,j} - 2u_{i,j} + u_{i-1,j}$$

$$\delta_x^2 u_{i,j} = u_{i+1,j} - 2u_{i,j} + u_{i-1,j} .$$

Using these formulas for the cell-face averages, the Fourier footprint of the flux integration for a cell is

$$
\begin{aligned}
\mathcal{F}(\Delta t\, Res) = &-\frac{i}{6} \left[\nu_x \sin\frac{\beta_x}{2} \left(13 \cos\frac{\beta_y}{2} - \cos\frac{3\beta_y}{2} \right) \right. \\
&\left. + \nu_y \sin\frac{\beta_y}{2} \left(13 \cos\frac{\beta_x}{2} - \cos\frac{3\beta_x}{2} \right) \right] \\
&-\frac{1}{6} \left[\theta_y \nu_x \sin\frac{\beta_x}{2} \left(\sin\frac{3\beta_y}{2} - 3\sin\frac{\beta_y}{2} \right) \right. \\
&\left. + \theta_x \nu_y \sin\frac{\beta_y}{2} \left(\sin\frac{3\beta_x}{2} - 3\sin\frac{\beta_x}{2} \right) \right] ,
\end{aligned}
$$

where the β's are the Fourier variables and the ν's are the Courant numbers

$$\nu_x = \frac{c_x \Delta t}{\Delta x}$$

$$\nu_y = \frac{c_y \Delta t}{\Delta y} .$$

To update the nodes, the cell-centered residual, given in Equation 2, multiplied by Δt, will be sent to the nodes (i,j), $(i+1,j)$, $(i+1,j+1)$ and $(i,j+1)$ with weights ω_{sw}, ω_{se}, ω_{ne}, and ω_{nw} respectively (see Figure 1). The Fourier footprint of this distribution step is given by

$$
\begin{aligned}
\mathcal{F}(Dist) = & \left[(\omega_{ne} + \omega_{sw}) \cos\frac{\beta_x + \beta_y}{2} \right. \\
&\left. + (\omega_{nw} + \omega_{se}) \cos\frac{\beta_x - \beta_y}{2} \right] \\
&+ i \left[(\omega_{sw} - \omega_{ne}) \sin\frac{\beta_x + \beta_y}{2} \right. \\
&\left. + (\omega_{nw} - \omega_{se}) \sin\frac{\beta_x - \beta_y}{2} \right] . \tag{5}
\end{aligned}
$$

If a simple forward-Euler time-stepping scheme is used, the net amplification factor for the entire scheme is

$$G(\nu_x, \nu_y, \beta_x, \beta_y) = 1 + \mathcal{F}(\Delta t Res)\,\mathcal{F}(Dist) \qquad (6)$$

The appropriate values for the θ's and the ω's remain to be determined from the stability analysis. The ω's correspond to convection directions, and should therefore be determined by enforcing stability for the long waves ($\beta_x, \beta_y \to 0$). The θ's control the high-order difference terms of the scheme, and should therefore be determined by enforcing stability for the short waves ($\beta_x, \beta_y \to \pi$).

Taking the limit of Equation 6 as $\beta_x, \beta_y \to 0$ yields the constraint

$$k^2 (\nu_x \beta_x + \nu_y \beta_y) =$$

$$(\omega_{sw} - \omega_{ne})\frac{\beta_x + \beta_y}{2} + (\omega_{nw} - \omega_{se})\frac{\beta_x - \beta_y}{2},$$

where k is some real constant. An added constraint (conservation) is that the entire residual must be distributed,

$$\omega_{ne} + \omega_{sw} + \omega_{nw} + \omega_{se} = 1.$$

Also, by symmetry, if the ν_x and ν_y are such that convection is directly towards one node, all of the residual is distributed to that node, i.e.

$$\omega_{ne} = 1 \quad \text{if} \quad \nu_x = \nu_y > 0;$$

$$\omega_{sw} = 1 \quad \text{if} \quad \nu_x = \nu_y < 0;$$

$$\omega_{nw} = 1 \quad \text{if} \quad -\nu_x = \nu_y > 0;$$

$$\omega_{se} = 1 \quad \text{if} \quad -\nu_x = \nu_y < 0.$$

Combining these conditions gives the distribution coefficients

$$\omega_{ne} = \max\left(0, \frac{(\nu_x + \nu_y)}{|\nu_x + \nu_y| + |\nu_x - \nu_y|}\right) \qquad (7)$$

$$\omega_{sw} = \max\left(0, \frac{-(\nu_x + \nu_y)}{|\nu_x + \nu_y| + |\nu_x - \nu_y|}\right) \qquad (8)$$

$$\omega_{nw} = \max\left(0, \frac{-(\nu_x - \nu_y)}{|\nu_x + \nu_y| + |\nu_x - \nu_y|}\right) \qquad (9)$$

$$\omega_{se} = \max\left(0, \frac{(\nu_x - \nu_y)}{|\nu_x + \nu_y| + |\nu_x - \nu_y|}\right). \qquad (10)$$

These formulas state that the residual is sent only to the nodes that define the downwind face, and is distributed in a weighted manner between the two nodes on that face. For a plane wave moving in one of the coordinate directions, the two downwind weights are equal, and the scheme reduces to the standard one-dimensional upwind scheme.
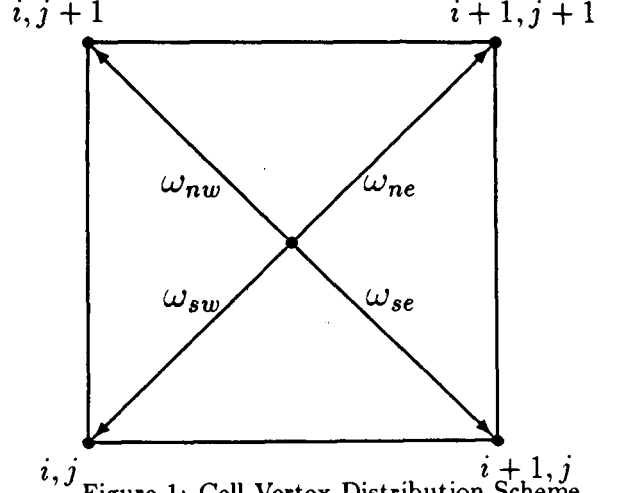

Figure 1: Cell-Vertex Distribution Scheme

A short-wave analysis shows that a necessary condition for stability is

$$(|\nu_x + \nu_y| - |\nu_x - \nu_y|)(\nu_x \theta_y + \nu_y \theta_x) > 0.$$

For this to hold for all values of ν_x and ν_y, the constraint

$$\frac{\theta_y}{\theta_x} = \frac{\nu_y}{\nu_x}$$

must be met, so that the θ's must be given by

$$\theta_x = \alpha' \nu_y$$

$$\theta_y = \alpha' \nu_x$$

For steady solutions that are independent of Δt, the θ's must be independent of Δt. This leads to the choice

$$\theta_x = \frac{\alpha \nu_x}{\max(|\nu_x|, |\nu_y|)} \qquad (11)$$

$$\theta_y = \frac{\alpha \nu_y}{\max(|\nu_x|, |\nu_y|)} \qquad (12)$$

where α is a positive parameter of order one. It is interesting to note that this says that the θ's must be *downwinded*, i.e., in the cell-face average calculation of Equations 3 and 4, the θ's must be chosen so as to give more influence to the second-difference about the downwind node of the face.

The only parameter in the scheme that remains to be determined is the value of α. Figures 3–5 show the effect of different values of α on the amplification factor G of the scheme. The maximum amplitude of the amplification factor over the high-frequency region (see Figure 2)

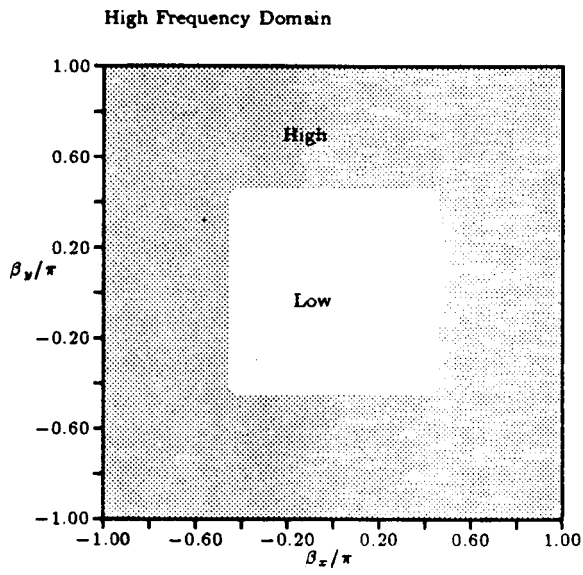$$G_{max}(\alpha) = \max_{|\beta_x|, |\beta_y| > \pi/2} \left| G(\beta_x, \beta_y, \nu_x, \nu_y, \alpha) \right|$$

High Frequency Domain

Figure 2: High-Frequency Region Used to Determine α
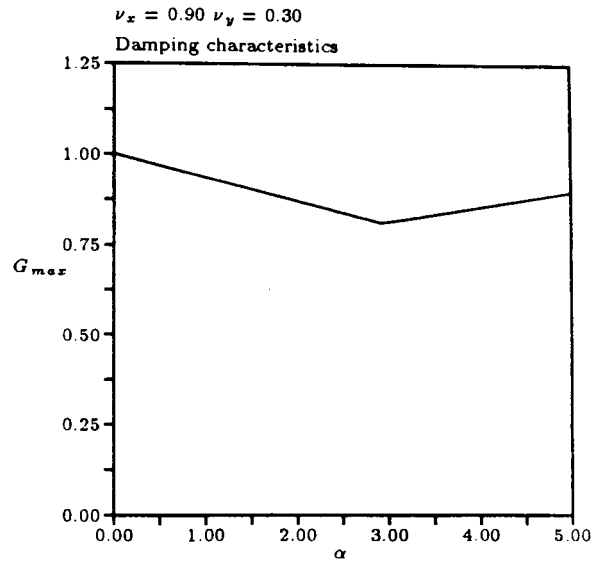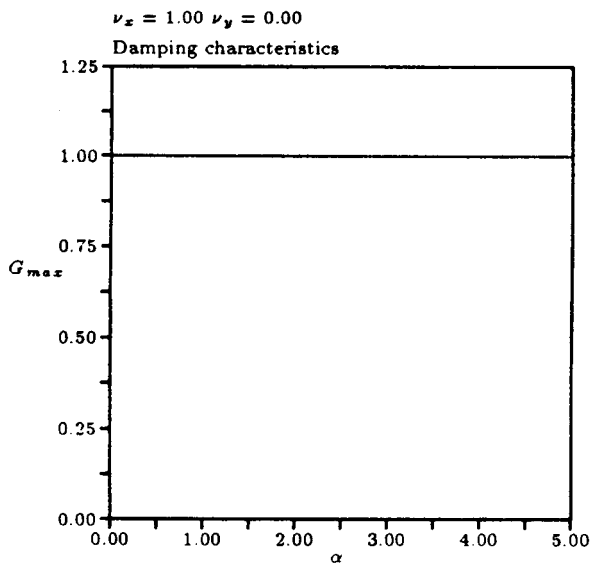
$\nu_x = 0.90 \; \nu_y = 0.30$

Damping characteristics

Figure 4: Effect of α on Stability — 20° Wave

$\nu_x = 1.00 \; \nu_y = 0.00$

Damping characteristics

Figure 3: Effect of α on Stability — 0° Wave

$\nu_x = 0.80 \; \nu_y = 0.80$

Damping characteristics

Figure 5: Effect of α on Stability — 45° Wave

4

New Cell-Vertex Scheme
Stability Boundary
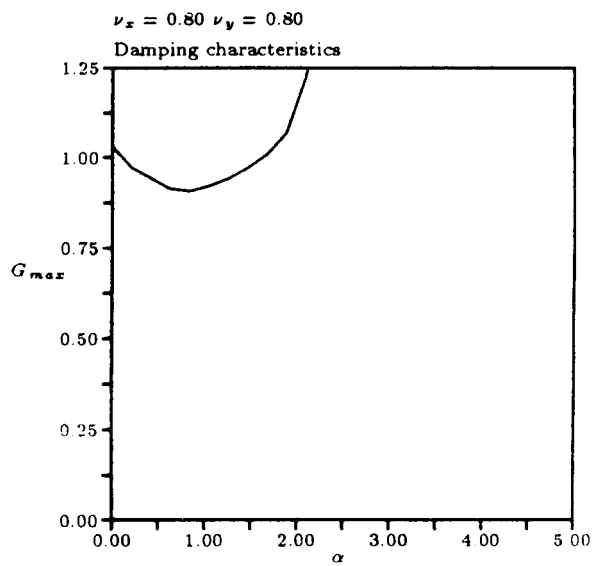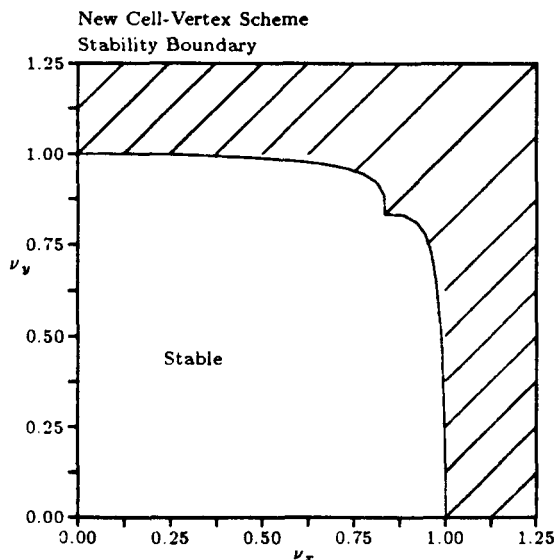
Figure 6: Stability Boundary for Scheme

$\nu_x = 1.00$ and $\nu_y = 0.00$

Figure 7: Fourier Footprint of Scheme — $0°$ wave

is plotted as a function of α for waves traveling at $0°$, $20°$ and $45°$. Based on these results, the value $\alpha = 1.0$ was chosen for the scheme. The stability boundary for the scheme, with $\alpha = 1.0$, is shown in Figure 6.

The locus of the scheme (i.e. the Fourier footprint of $F(\Delta t Res)F(Dist)$) is shown for the $0°$, $20°$ and $45°$ waves in Figures 7–9. The plots are generated by varying β_x continuously and β_y discretely, which leads to a mesh of points within the continuous footprint of the locus. The actual locus of the scheme consists of the lines in the plot, and all the space between the lines. The circular stablity boundary of forward-Euler time-stepping is circumscribed about the loci for reference. The loci are very different from those of first-order upwind or central-difference schemes. It is the wave that is convected at $45°$ that is damped the best, while waves at $0°$ (or $90°$) are not damped well. This can be seen clearly in the contours of the amplification factor for the scheme, shown in Figures 10–12.

Some numerical results for a convected Gaussian on a 32 × 32 grid are given in Figures 13–15. In each case the Gaussian propagates across the grid virtually undistorted. The onset of a zebra instability can be seen in the $0°$ case, as predicted in the stability analysis. The amplitude of oscillations in this case is very small (on the order of 10^{-4}). The convergence history for each of the cases is shown in Figures 16–18. The Gaussian convects at almost one cell per iteration, so that the slope of the residual curve changes drastically after approximately forty iterations. The $45°$ case, which has the best high-frequency damping, converges very quickly, while the $0°$ case converges very slowly. Table 1 shows the results of a grid-refinement study confirming the third-order accuracy of the scheme.
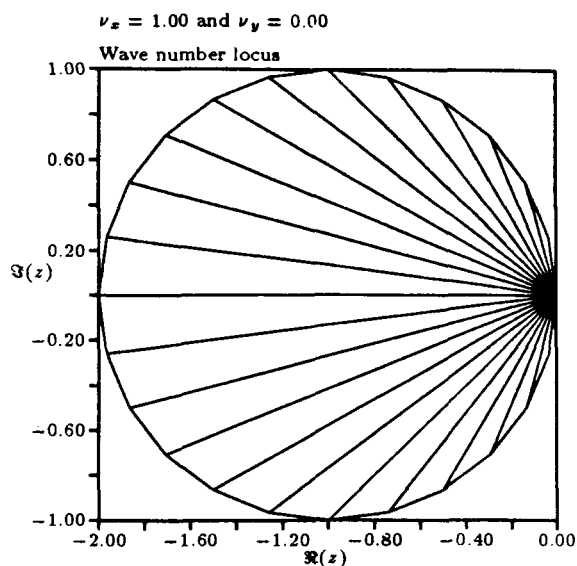

$\nu_x = 0.90$ and $\nu_y = 0.30$
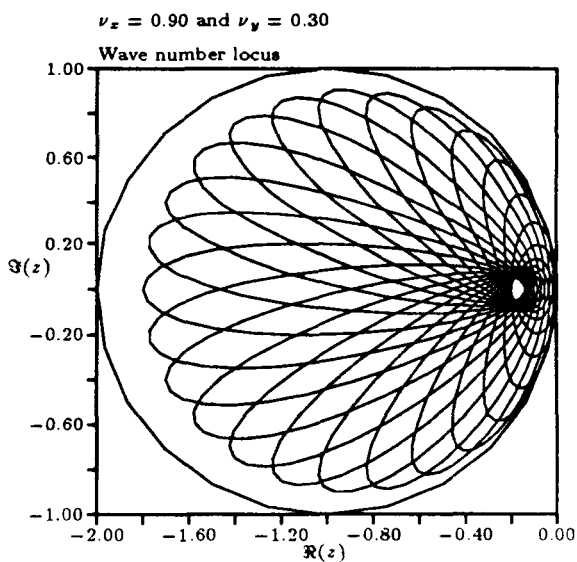
Figure 8: Fourier Footprint of Scheme — $20°$ wave

5

$\nu_x = 0.80$ and $\nu_y = 0.80$

Wave number locus
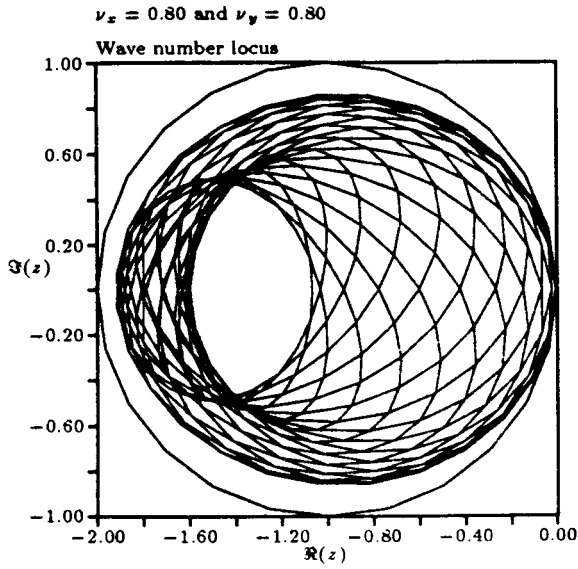
Figure 9: Fourier Footprint of Scheme — 45° wave

$\nu_x = 0.90$ and $\nu_y = 0.30$

Amplification factor

1	0.0000
2	0.1000
3	0.2000
4	0.3000
5	0.4000
6	0.5000
7	0.6000
8	0.7000
9	0.8000
10	0.9000
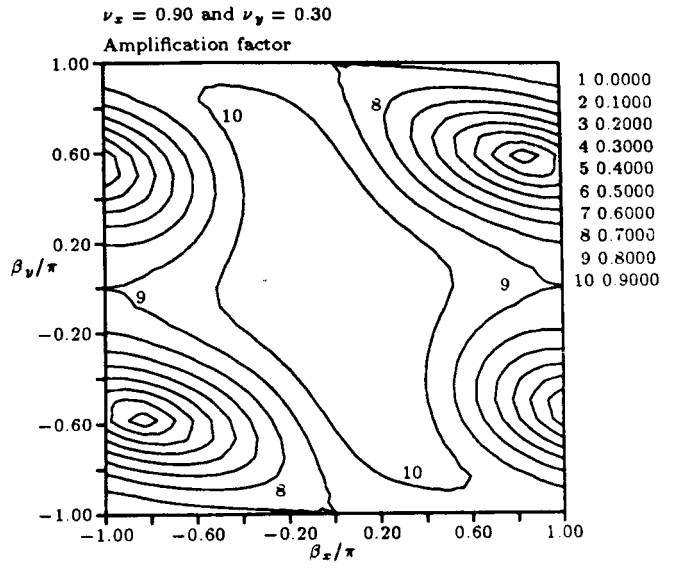
Figure 11: Amplification Factor of Scheme — 20° wave

$\nu_x = 1.00$ and $\nu_y = 0.00$

Amplification factor

1	0.0000
2	0.1000
3	0.2000
4	0.3000
5	0.4000
6	0.5000
7	0.6000
8	0.7000
9	0.8000
10	0.9000
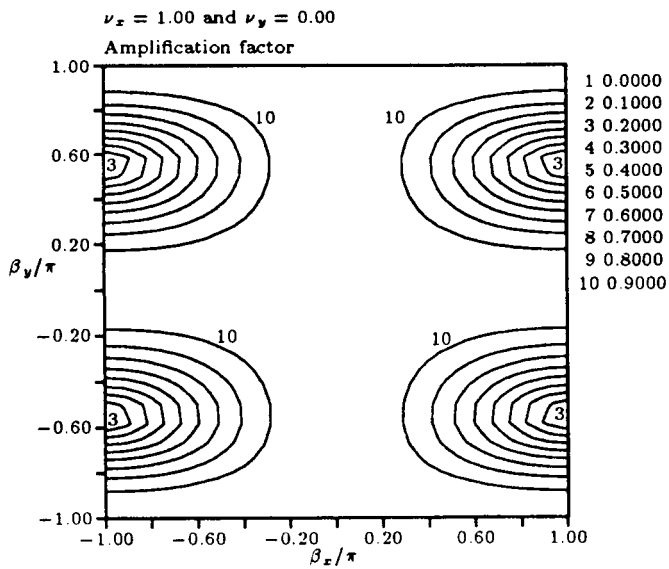
Figure 10: Amplification Factor of Scheme — 0° wave

$\nu_x = 0.80$ and $\nu_y = 0.80$

Amplification factor

1	0.0000
2	0.1000
3	0.2000
4	0.3000
5	0.4000
6	0.5000
7	0.6000
8	0.7000
9	0.8000
10	0.9000
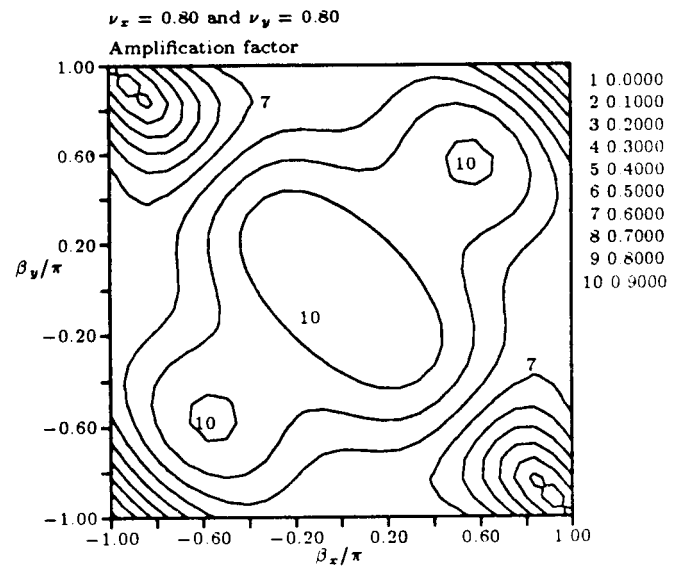
Figure 12: Amplification Factor of Scheme — 45° wave

6

$\nu_x = 1.00 \; \nu_y = 0.00 \; \xi = 0.25$

Convected Gaussian

1	0.0000
2	0.1000
3	0.2000
4	0.3000
5	0.4000
6	0.5000
7	0.6000
8	0.7000
9	0.8000
10	0.9000
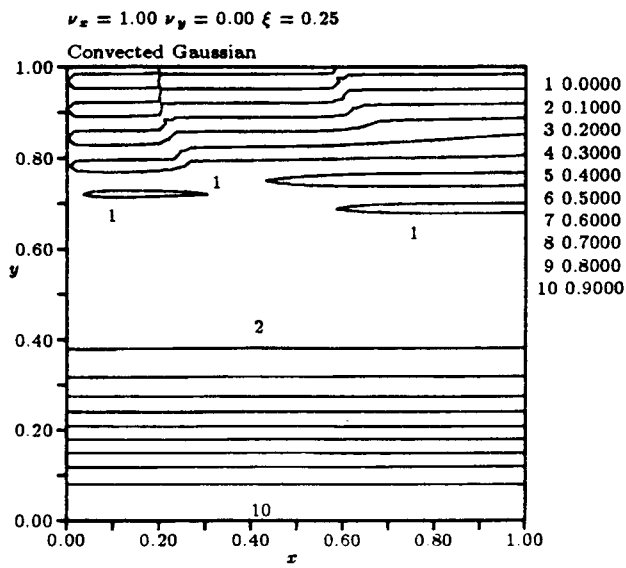
Figure 13: Gaussian Convected at 0°

$\nu_x = 0.80 \; \nu_y = 0.80 \; \xi = 0.25$

Convected Gaussian

1	0.0000
2	0.1000
3	0.2000
4	0.3000
5	0.4000
6	0.5000
7	0.6000
8	0.7000
9	0.8000
10	0.9000
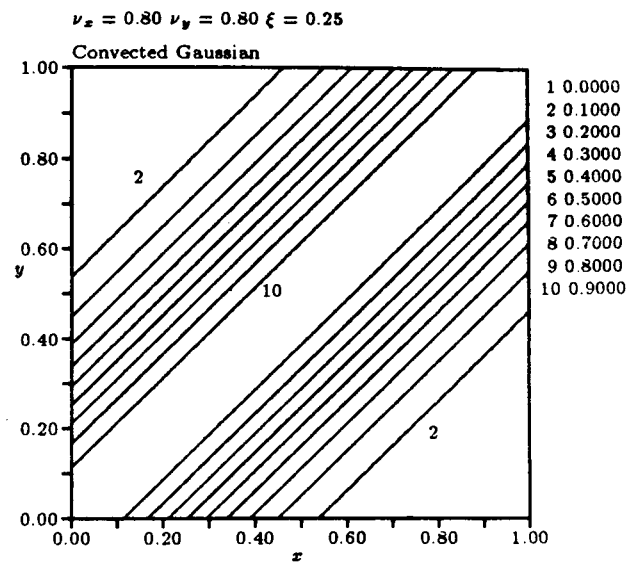
Figure 15: Gaussian Convected at 45°

$\nu_x = 0.90 \; \nu_y = 0.30 \; \xi = 0.25$

Convected Gaussian

1	0.0000
2	0.1000
3	0.2000
4	0.3000
5	0.4000
6	0.5000
7	0.6000
8	0.7000
9	0.8000
10	0.9000
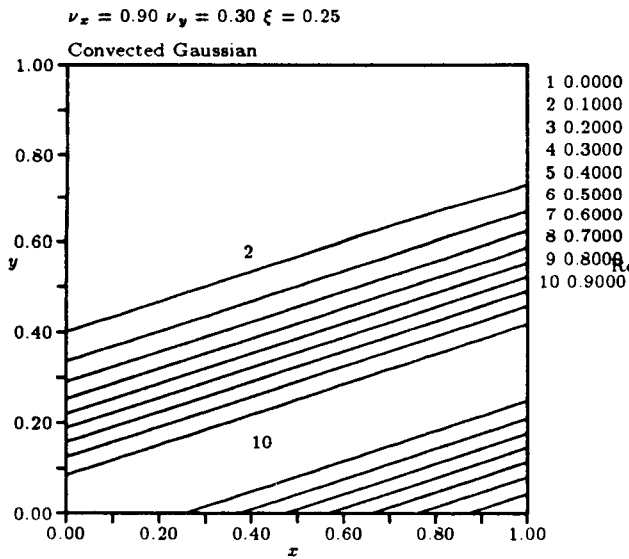
Figure 14: Gaussian Convected at 20°

$\nu_x = 1.00 \; \nu_y = 0.00 \; \xi = 0.25$

Convergence History

Residual
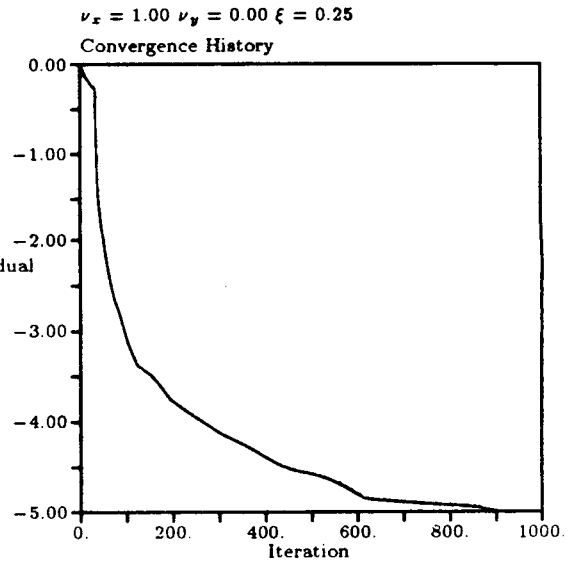
Figure 16: Convergence History for 0° Case
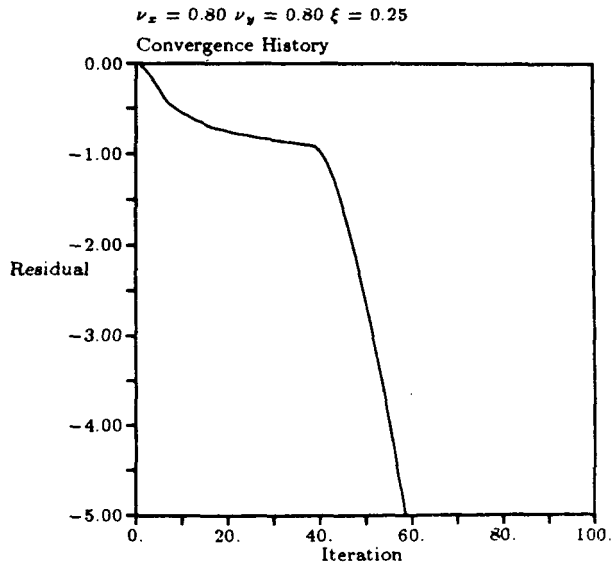
7
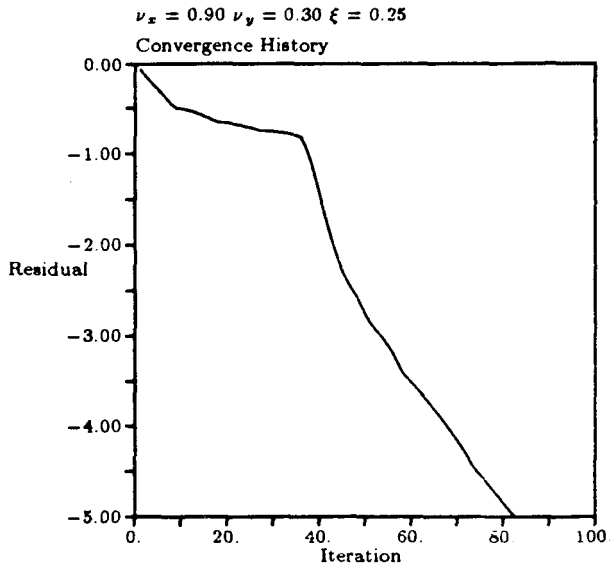
Figure 17: Convergence History for 20° Case

Figure 18: Convergence History for 45° Case

Grid	Peak at $x = 0.5$	Estimated Order
4^2	0.84602	–
8^2	0.95929	1.92
16^2	0.99314	2.57
32^2	0.99907	2.88
64^2	0.99988	2.95

Table 1: Order of Accuracy Study — Convection of Unit-Amplitude Gaussian, $\xi = 0.25$, at 45°

Scheme for the Euler Equations

The Euler equations are

$$\frac{\partial \mathbf{U}}{\partial t} + \frac{\partial \mathbf{F}}{\partial x} + \frac{\partial \mathbf{G}}{\partial y} = 0, \qquad (13)$$

where $\mathbf{U}$ is the state vector of conserved variables

$$\mathbf{U} = \left\{ \begin{array}{c} \rho \\ \rho u \\ \rho v \\ \rho E \end{array} \right\}$$

and $\mathbf{F}$ and $\mathbf{G}$ are the flux vectors

$$\mathbf{F} = \left\{ \begin{array}{c} \rho u \\ \rho u^2 + p \\ \rho u v \\ \rho u (E + p/\rho) \end{array} \right\} \quad \mathbf{G} = \left\{ \begin{array}{c} \rho v \\ \rho u v \\ \rho v^2 + p \\ \rho v (E + p/\rho) \end{array} \right\} .$$

To solve the Euler equations with a scheme analagous to the one above, the system must be decomposed into a set of two-dimensional convection equations, with or without source terms. Once the equations have been decomposed, each component can be treated with the convection scheme described above. The distribution step carries over in a very straightforward manner; the flux calculation (particularly the higher-order terms) must be treated carefully to ensure that the formulation for the system is consistent with the formulation for the scalar equation, and that the resulting scheme is conservative.

Decomposition of the Euler Equations

Roe [2,12] has formulated a decomposition of the two-dimensional Euler equations, based on the eigenvectors of the matrix

$$\hat{\mathbf{A}} = \frac{\partial \mathbf{F}}{\partial \mathbf{U}} \cos \theta + \frac{\partial \mathbf{G}}{\partial \mathbf{U}} \sin \theta$$

The eigenvectors of $\hat{\mathbf{A}}$ represent a shear wave, a contact discontinuity and two acoustic waves. Roe makes use of these eigenvectors, decomposing the flow into, for example, four acoustic waves, one shear wave and an entropy wave. He uses local values of the flow gradients to compute the strength and angle of inclination of each of the waves in his model.

Hirsch et al. [1] have formulated a different decomposition, which converts the Euler equations to the form

$$\frac{\partial \mathbf{W}^*}{\partial t} + \mathbf{D_x} \frac{\partial \mathbf{W}^*}{\partial x} + \mathbf{D_y} \frac{\partial \mathbf{W}^*}{\partial y} = \mathbf{S},$$

where $\mathbf{W}^*$ is a vector of convected quantities (entropy, a component of velocity, and two acoustic-like variables),

8

D_x and D_y are diagonal matrices of convection speeds, and S is a source term. Similarly to Roe's decomposition, the decomposition of Hirsch is based on the matrix

$$\hat{A} = \frac{\partial F}{\partial U}\cos\theta + \frac{\partial G}{\partial U}\sin\theta$$

$$= \frac{\partial F}{\partial U}\kappa_x + \frac{\partial G}{\partial U}\kappa_y$$

where κ_x and κ_y are the components of a unit propagation vector. Diagonalization of $\hat{A}$ gives

$$\hat{A} = PD(\kappa)P^{-1}$$

where

$$D(\kappa) = \begin{bmatrix} u\cdot\kappa & 0 & 0 & 0 \\ 0 & u\cdot\kappa & 0 & 0 \\ 0 & 0 & u\cdot\kappa+c & 0 \\ 0 & 0 & 0 & u\cdot\kappa-c \end{bmatrix}$$

and P and P^{-1} are the left- and right-eigenvector matrices. The choice of the unit vector κ is based on local flow gradients. Hirsh chooses κ so as to minimize the components of the source term S. To minimize all components, one needs *two* different κ vectors; $\kappa^{(1)}$ for the velocity-component convection and $\kappa^{(2)}$ for the acoustic-like convection. With two κ vectors,

$$\Delta W^* = \left\{ \begin{array}{c} \Delta p - \frac{\Delta\rho}{c^2} \\ \kappa_y^{(1)}\Delta u - \kappa_x^{(1)}\Delta v \\ \kappa^{(2)}\cdot\Delta u - \frac{\Delta p}{\rho c} \\ -\kappa^{(2)}\cdot\Delta u - \frac{\Delta p}{\rho c} \end{array} \right\}$$

and

$$D_x = \begin{bmatrix} u & 0 & 0 & 0 \\ 0 & u & 0 & 0 \\ 0 & 0 & u+\kappa_x^{(2)}c & 0 \\ 0 & 0 & 0 & u-\kappa_y^{(2)}c \end{bmatrix}$$

$$D_y = \begin{bmatrix} v & 0 & 0 & 0 \\ 0 & v & 0 & 0 \\ 0 & 0 & v+\kappa_y^{(2)}c & 0 \\ 0 & 0 & 0 & v-\kappa_y^{(2)}c \end{bmatrix}$$

and

$$S = \left\{ \begin{array}{c} 0 \\ -\frac{c}{2}\left(\kappa_y^{(1)}\frac{\partial}{\partial x} - \kappa_x^{(1)}\frac{\partial}{\partial y}\right)(W_3^* + W_4^*) \\ -c\left(\kappa_y^{(2)}\frac{\partial}{\partial x} - \kappa_x^{(2)}\frac{\partial}{\partial y}\right)W_2^* \\ -c\left(\kappa_y^{(2)}\frac{\partial}{\partial x} - \kappa_x^{(2)}\frac{\partial}{\partial y}\right)W_2^* \end{array} \right\}$$

These equations are general, holding for any choices of $\kappa^{(1)}$ and $\kappa^{(2)}$. Hirsch shows that, in order to minimze th source terms, one needs a $\kappa^{(1)}$ that is aligned locally with the pressure gradient, and a $\kappa^{(2)}$ that is related to the strain-rate tensor. That is, $\kappa^{(1)}$ is given by

$$\kappa^{(1)} = \frac{\nabla p}{|\nabla p|}$$

and $\kappa^{(2)}$ is computed from the velocity derivatives in the following way: if

$$\left(\frac{\partial v}{\partial x} + \frac{\partial u}{\partial y}\right)^2 - 4\frac{\partial u\partial x}{\partial v\partial y} \leq 0$$

then the propagation angle

$$\tan\theta = \frac{\frac{\partial v}{\partial x} + \frac{\partial u}{\partial y}}{2\frac{\partial u}{\partial x}}$$

is calculated; otherwise, the possible propagation angles are given by

$$\tan\theta = \frac{\left(\frac{\partial v}{\partial x} + \frac{\partial u}{\partial y}\right) \pm \sqrt{\left(\frac{\partial v}{\partial x} + \frac{\partial u}{\partial y}\right)^2 - 4\frac{\partial u}{\partial x}\frac{\partial v}{\partial y}}}{2\frac{\partial u}{\partial x}}. \quad (14)$$

The value of $\kappa^{(2)}$ is then

$$\kappa^{(2)} = \cos\theta\,i + \sin\theta\,j.$$

The proper branch for Equation 14 is the one that maximizes the inner product $\kappa^{(1)}\cdot\kappa^{(2)}$. This inner product appears in the denominator of entries of the transformation matrix P^* (described below); the two vectors therefore must not be perpendicular. This is ensured by taking $\kappa^{(2)} := \kappa^{(1)}$ if the nominal value of the inner product is less than $1/10$.

Hirsch's decomposition was chosen for this study because the matrix P^* is square (4×4), as opposed to Roe's decomposition, which yields a 6×4 matrix.

Extension of Convection Scheme

Just as in the scheme for the convection equation, the scheme for the Euler equations is made up of two primary steps:

1. a residual calculation based on a flux integral;

2. a residual distribution.

Each of these steps is somewhat more complicated for the system, however.

For the Euler equations, the residual for a cell is given by

$$\mathbf{Res}_{i+\frac{1}{2},j+\frac{1}{2}} = -\frac{1}{A} \oint_{\partial A} [\mathbf{F}\,dy - \mathbf{G}\,dx] \,, \qquad (15)$$

where A is the cell area and the integral is taken along the cell's boundary ∂A. The cells are now quadrilaterals, with faces lying along curvilinear coordinate lines $\xi = \xi_i$ and $\eta = \eta_j$. The boundary integral of Equation 15 is composed of contributions of fluxes normal to cell faces. To extend the approximation of Equations 3 and 4 so that they apply to the above residual, it is necessary to convert these to flux approximations. Equation 4, for instance, when multiplied by $c_x \Delta y$, becomes an expression for the total flux across the cell-face centered at $(i, j + 1/2)$:

$$
\begin{aligned}
c_x u_{i,j+\frac{1}{2}} \Delta y \;=\;& \frac{c_x u_{i,j} + c_x u_{i,j+1}}{2} \Delta y \\
& -\frac{\delta_y^2}{12}\left\{ \frac{c_x u_{i,j} + c_x u_{i,j+1}}{2} \Delta y \right. \\
& \left. +\frac{1}{2}\theta_y c_x \left(u_{i,j+1} - u_{i,j}\right)\Delta y \right\} \,.
\end{aligned}
$$

With regard to the Euler equations, this translates directly into

$$
\begin{aligned}
\hat{\mathbf{F}}_{i,j+\frac{1}{2}} \Delta\eta \;=\;& \frac{\mathbf{F}_{i,j} + \mathbf{F}_{i,j+1}}{2} \Delta_\eta y - \frac{\mathbf{G}_{i,j} + \mathbf{G}_{i,j+1}}{2} \Delta_\eta x \\
& -\frac{\delta_\eta^2}{12}\left\{ \frac{\mathbf{F}_{i,j} + \mathbf{F}_{i,j+1}}{2} \Delta_\eta y - \frac{\mathbf{G}_{i,j} + \mathbf{G}_{i,j+1}}{2} \Delta_\eta x \right. \\
& +\frac{1}{2}\left(\boldsymbol{\Theta}_\eta\right)_{i,j+\frac{1}{2}} \left[\left(\mathbf{F}_{i,j+1} - \mathbf{F}_{i,j}\right)\Delta_\eta y \right. \\
& \left.\left. -\left(\mathbf{G}_{i,j+1} - \mathbf{G}_{i,j}\right)\Delta_\eta x\right] \right\} \,,
\end{aligned}
$$

in which the following notation is used:

$$
\begin{aligned}
\Delta_\eta x \;&=\; x_{i,j+1} - x_{i,j} \\
\Delta_\eta y \;&=\; y_{i,j+1} - y_{i,j} \\
\Delta\eta \;&=\; \eta_{j+1} - \eta_j
\end{aligned}
$$

The quantity $\hat{\mathbf{F}}$ denotes the flux normal to a cell-face, scaled such that

$$\hat{\mathbf{F}}\,d\eta = \mathbf{F}\,dy - \mathbf{G}\,dx \,.$$

The matrix $\boldsymbol{\Theta}_\eta$ replaces the scalar θ_y; it acts as a scalar in each of the convection equations generated by the transformation matrix $\mathbf{P}^*$

$$\boldsymbol{\Theta}_\eta = \mathbf{P}^* \mathrm{diag}\left\{\theta_\eta^{(k)}\right\} \mathbf{P}^{*-1} \,, \qquad (16)$$

with

$$\theta_\eta^{(k)} = \frac{\alpha\nu_\eta^{(k)}}{\max\left(\left|\nu_\xi^{(k)}\right|, \left|\nu_\eta^{(k)}\right|\right)} \,.$$

The contravariant Courant numbers $\nu_\xi^{(k)}$ and $\nu_\eta^{(k)}$ and the transformation matrix $\mathbf{P}^*$ are defined further below. Note that $\mathbf{P}^*$ and $\theta_\xi^{(k)}$ are defined per cell, and must be averaged over neighboring cells to yied a cell-face value.

The analog of Equation 3 is

$$
\begin{aligned}
\hat{\mathbf{G}}_{i+\frac{1}{2},j} \Delta\xi \;=\;& \frac{\mathbf{F}_{i,j} + \mathbf{F}_{i+1,j}}{2} \Delta_\xi y - \frac{\mathbf{G}_{i,j} + \mathbf{G}_{i+1,j}}{2} \Delta_\xi x \\
& -\frac{\delta_\xi^2}{12}\left\{ \frac{\mathbf{F}_{i,j} + \mathbf{F}_{i+1,j}}{2} \Delta_\xi y - \frac{\mathbf{G}_{i,j} + \mathbf{G}_{i+1,j}}{2} \Delta_\xi x \right. \\
& +\frac{1}{2}\left(\boldsymbol{\Theta}_\xi\right)_{i+\frac{1}{2},j} \left[\left(\mathbf{F}_{i+1,j} - \mathbf{F}_{i,j}\right)\Delta_\xi y \right. \\
& \left.\left. -\left(\mathbf{G}_{i+1,j} - \mathbf{G}_{i,j}\right)\Delta_\xi x\right] \right\}
\end{aligned}
$$

with

$$
\begin{aligned}
\Delta_\xi x \;&=\; x_{i+1,j} - x_{i,j} \\
\Delta_\xi y \;&=\; y_{i+1,j} - y_{i,j} \\
\Delta\xi \;&=\; \xi_{i+1} - \xi_i
\end{aligned}
$$

and

$$\hat{\mathbf{G}}\,d\xi = \mathbf{F}\,dy - \mathbf{G}\,dx \,.$$

The matrix $\boldsymbol{\Theta}_\xi$ is given by

$$\boldsymbol{\Theta}_\xi = \mathbf{P}^* \mathrm{diag}\left\{\theta_\xi^{(k)}\right\} \mathbf{P}^{*-1} \,, \qquad (17)$$

with

$$\theta_\xi^{(k)} = \frac{\alpha\nu_\xi^{(k)}}{\max\left(\left|\nu_\xi^{(k)}\right|, \left|\nu_\eta^{(k)}\right|\right)} \,.$$

The contravariant Courant numbers $\nu_\xi^{(k)}$ and $\nu_\eta^{(k)}$ are related to the wave speeds normal to the cell faces. Thus we have, for instance,

$$\left(\nu_\xi^{(k)}\right)_{i+\frac{1}{2},j+\frac{1}{2}} = \frac{\Delta t}{A} \left(c_x \Delta_\eta y - c_y \Delta_\eta x\right)_{i+\frac{1}{2},j+\frac{1}{2}} \,, \quad (18)$$

with

$$\left(\Delta_\eta x\right)_{i+\frac{1}{2},j+\frac{1}{2}} = \frac{1}{2}\left(x_{i,j+1} - x_{i,j} + x_{i+1,j+1} - x_{i+1,j}\right)$$

$$\left(\Delta_\eta y\right)_{i+\frac{1}{2},j+\frac{1}{2}} = \frac{1}{2}\left(y_{i,j+1} - y_{i,j} + y_{i+1,j+1} - y_{i+1,j}\right) \,.$$

The Cartesian wave speeds c_x and c_y are the diagonal elements of the matrices $\mathbf{D_x}$ and $\mathbf{D_y}$ introduced previously, and are evaluated at $(i + 1/2, y + 1/2)$ by using cell-averaged state quantities and the cell-centered κ values. Note that the factor Δt in Equation 18 drops

10

out in the definition of $\theta_\xi^{(k)}$. Analagous to Equation 18 is

$$\left(\nu_\eta^{(k)}\right)_{i+\frac{1}{2},j+\frac{1}{2}} = \frac{\Delta t}{A}\left(c_x\Delta_\xi y - c_y\Delta_\xi x\right)_{i+\frac{1}{2},j+\frac{1}{2}}, \quad (19)$$

with

$$\left(\Delta_\xi x\right)_{i+\frac{1}{2},j+\frac{1}{2}} = \frac{1}{2}\left(x_{i+1,j} - x_{i,j} + x_{i+1,j+1} - x_{i,+1j}\right)$$

$$\left(\Delta_\xi y\right)_{i+\frac{1}{2},j+\frac{1}{2}} = \frac{1}{2}\left(y_{i+1,j} - y_{i,j} + y_{i+1,j+1} - y_{i,j+1}\right).$$

The transformation matrix $\mathbf{P}^*$ is given, in columns, by

$$\mathbf{P}^{*(1)} = \begin{bmatrix} 1 \\ u \\ v \\ \frac{u^2+v^2}{2} \end{bmatrix}$$

$$\mathbf{P}^{*(2)} = \begin{bmatrix} 0 \\ \frac{\rho\kappa_y^{(2)}}{\kappa^{(1)}\cdot\kappa^{(2)}} \\ -\frac{\rho\kappa_y^{(2)}}{\kappa^{(1)}\cdot\kappa^{(2)}} \\ \frac{\rho u\kappa_y^{(2)}-\rho v\kappa_x^{(2)}}{\kappa^{(1)}\cdot\kappa^{(2)}} \end{bmatrix}$$

$$\mathbf{P}^{*(3)} = \begin{bmatrix} \frac{\rho}{2c} \\ \frac{\rho}{2c\kappa^{(1)}\cdot\kappa^{(2)}}\left(u\kappa^{(1)}\cdot\kappa^{(2)}+c\kappa_x^{(1)}\right) \\ \frac{\rho}{2c\kappa^{(1)}\cdot\kappa^{(2)}}\left(v\kappa^{(1)}\cdot\kappa^{(2)}+c\kappa_y^{(1)}\right) \\ \frac{\rho}{2c\kappa^{(1)}\cdot\kappa^{(2)}}\left(H\kappa^{(1)}\cdot\kappa^{(2)}+c\mathbf{u}\cdot\kappa^{(1)}\right) \end{bmatrix}$$

$$\mathbf{P}^{*(4)} = \begin{bmatrix} \frac{\rho}{2c} \\ \frac{\rho}{2c\kappa^{(1)}\cdot\kappa^{(2)}}\left(u\kappa^{(1)}\cdot\kappa^{(2)}-c\kappa_x^{(1)}\right) \\ \frac{\rho}{2c\kappa^{(1)}\cdot\kappa^{(2)}}\left(v\kappa^{(1)}\cdot\kappa^{(2)}-c\kappa_y^{(1)}\right) \\ \frac{\rho}{2c\kappa^{(1)}\cdot\kappa^{(2)}}\left(H\kappa^{(1)}\cdot\kappa^{(2)}-c\mathbf{u}\cdot\kappa^{(1)}\right) \end{bmatrix}$$

The distribution step requires, in each cell, projection of the residual onto the columns of the matrix $\mathbf{P}^*$, giving weights $r^{(k)}$, and multiplication of each of the resulting vectors by an appropriate time-step:

$$\mathbf{Res}_{i+\frac{1}{2},j+\frac{1}{2}} = \sum_{k=1}^{4}\left(r^{(k)}\mathbf{P}^{*(k)}\right)_{i+\frac{1}{2},j+\frac{1}{2}} \quad (20)$$

$$\delta_t\mathbf{U}^{(k)}_{i+\frac{1}{2},j+\frac{1}{2}} = \left(\Delta t^{(k)}r^{(k)}\mathbf{P}^{*(k)}\right)_{i+\frac{1}{2},j+\frac{1}{2}}, \quad (21)$$

where k varies from one to four. In the above, $\mathbf{P}^{*(k)}$ denotes the kth column of $\mathbf{P}^*$, corresponding to the kth wave, and $\delta_t\mathbf{U}^{(k)}$ is the portion of time change in the state vector caused by the kth wave. Each $\delta_t\mathbf{U}^{(k)}$ may be divided between the two vertices of the downwind cell-face, according to the weights of Equations 7–10, with ν_x and ν_y replaced by $\nu_\xi^{(k)}$ and $\nu_\eta^{(k)}$, e.g.

$$\omega_{ne}^{(k)} = \max\left(0, \frac{\left(\nu_\xi^{(k)}+\nu_\eta^{(k)}\right)}{\left|\nu_\xi^{(k)}+\nu_\eta^{(k)}\right|+\left|\nu_\xi^{(k)}-\nu_\eta^{(k)}\right|}\right).$$

As indicated in Equation 21, it is not necessary to take the same value of Δt for each cell, or even for each wave. Spatial conservation, and, therefore, the ability to find steady weak solutions, is guaranteed by formulating the discrete residual on the basis of Equation 15. Using different time steps in different cells is a well-known technique called "local time-stepping;" using different time steps for different waves is new, and will be called "characteristic time-stepping." Mathematically speaking, the use of a non-constant Δt is equivalent to preconditioning the equations. Local time-stepping takes away the stiffness due to spatial variations, and may be called "spatial preconditioning;" characteristic time-stepping removes the stiffness due to the differences among the local wave speeds, and may be called "wave-preconditioning."

In local time-stepping, one chooses, with some safety margin, the largest single time-step value that satisfies the stability criterion (see Figure 6) for the local values of all pairs $\nu_\xi^{(k)}, \nu_\eta^{(k)}$. In characteristic time-stepping, the time-step for each pair is maximized separately. The validity of this practice hinges on the assumption that, in the steady state, each residual (Equation 15) vanishes separately; for a cell-vertex scheme this, however, is not generally true. All one can assume is that the sum of all residual components sent to a particular vertex vanishes in the steady state. To prevent an imbalance among contributions $\delta_t\mathbf{U}^{(k)}$ for a particular k, arriving in a vertex from different cells, both local and characteristic time-step values need to be assigned to vertices (i,j) rather than cell-centers $(i+1/2, j+1/2)$.

The use of characteristic time steps requires special provisions near sonic lines, steady shocks and stagnation points, i.e. in regions where one of the convection speeds vanishes. The linear stability criterion then allows of arbitrarily large values of Δt; in practice, however, its value must be constrained by a solution-dependent upper limit. How to do this robustly in the multi-dimensional case is not yet known; for one-dimensional flow, some progress has been reported [13].

Boundary conditions are imposed at the walls by enforcing a tangency condition at the vertices on the walls and zeroing the mass-flux for the faces on the walls. Boundary conditions at inflow and outflow are imposed by a non-reflecting condition described by Lindquist and Giles [14].

11

Results

The scheme described above was used to compute steady flows in a two-dimensional channel, with cosine-shaped walls yielding a 10% constriction at the throat. Two different inflow Mach numbers were taken;

1. $M_\infty = 1.75$;

2. $M_\infty = 3.50$.

Both cases were run on the 64 × 32 grid shown in Figure 19. It is worth mentioning here that the full grid was used in the calculations: although the final steady state is symmetric about the channel axis, the transient states are not, due to the asymmetry of the $\kappa^{(2)}$. This asymmetry of the Hirsch decomposition is suspected to have a negative effect on the convergence to a steady state; this remains to be investigated. In comparison, the decomposition of Roe preserves flow symmetry.

The results for the first case are shown in Figures 20–30. Figure 20 shows the Mach number contours of the steady flow. The compression waves caused by the cosine bump, the coalescence into shock waves, and the reflection of the shocks are clearly seen. There are some oscillations at the shocks, due to the fact that the scheme is third-order accurate everywhere. For comparison, results from a grid-biased cell-centered upwind scheme [15] are shown in Figures 21 and 22. This scheme is linearly third-order accurate but formally third-order accurate only for one-dimensional flow; the approximate Riemann solver used for upwinding is Osher's. Figure 21 shows the results produced without limiting of higher-order terms, allowing a fair comparison with Figure 20. The results are very similar, the cell-centered scheme being a little less oscillatory, but yielding less defined reflected shocks. The results of Figure 22 were rendered monotone by the use of Van Albada's limiter [16], leading to a clear loss of resolution for all waves, especially the reflected shocks. The remaining plots show the details of the shock-intersection region. Figure 23 shows the grid in this region; Figure 24 shows the Mach number contours. Comparison of the two shows that, although the shock is oblique to the grid, it is everywhere captured across two cells. The $\kappa^{(1)}$ vectors (related to the pressure-gradient) and the $\kappa^{(2)}$ vectors (related to the strain-rate tensor) are shown in Figures 25 and 26. These give rise to the convection directions shown in Figures 27–29. The first shows the convection direction for the shear variable and the entropy variable; this is simply the stream direction. The remaining two show the convection directions for the acoustic-like variables. The shocks are evident in the acoustic directions. Convergence histories for this case are shown in Figure 30. The two different convergence rates are for:

1. constant Δt (no preconditioning);

2. a different Δt in each cell (spatial preconditioning).
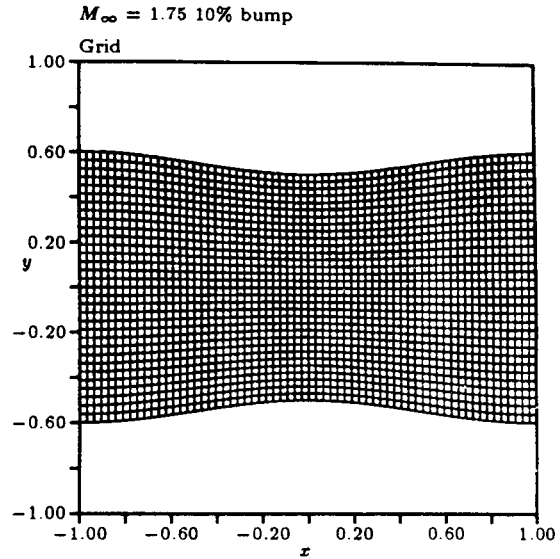
Figure 19: $M_\infty = 1.75$ Case — Grid
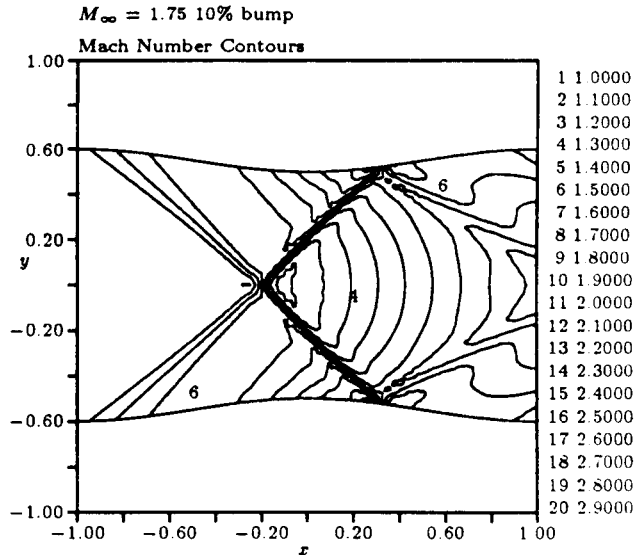
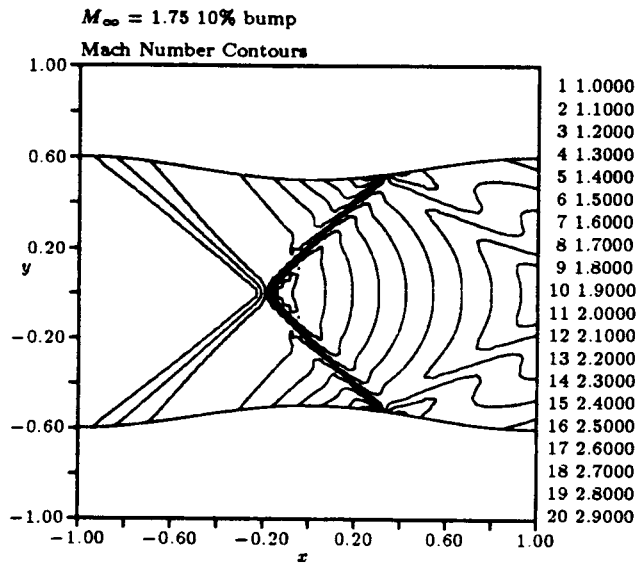Figure 20: $M_\infty = 1.75$ Case — Mach Number Contours

Figure 21: $M_\infty = 1.75$ Case — Grid-Biased Upwind Results (Limiter Off)
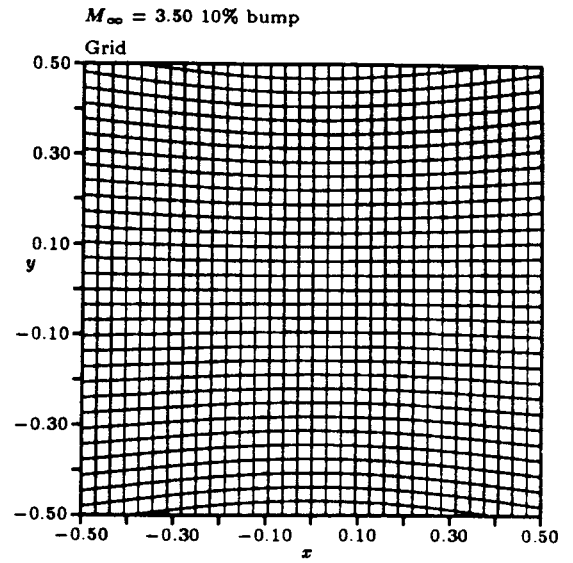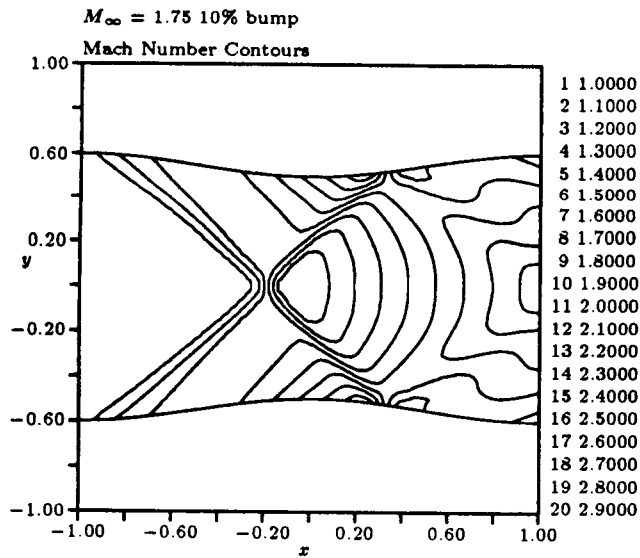

Figure 23: $M_\infty = 1.75$ Case — Grid

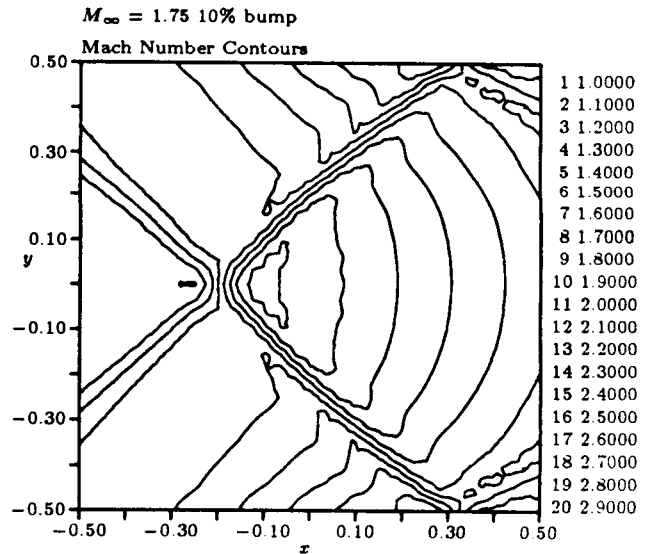Figure 22: $M_\infty = 1.75$ Case — Grid-Biased Upwind Results (Limiter On)

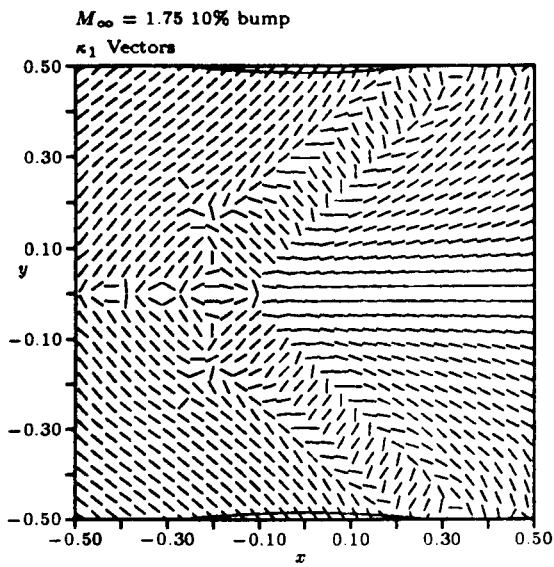Figure 24: $M_\infty = 1.75$ Case — Mach Number Contours
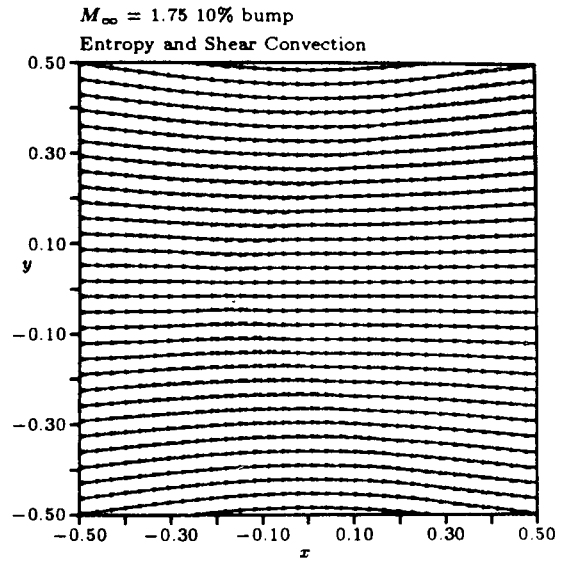
13

$M_\infty = 1.75$ 10% bump
κ_1 Vectors

Figure 25: $M_\infty = 1.75$ Case — $\kappa^{(1)}$ Directions

$M_\infty = 1.75$ 10% bump
Entropy and Shear Convection

Figure 27: $M_\infty = 1.75$ Case — Convection Directions for Shear and Entropy

$M_\infty = 1.75$ 10% bump
κ_2 Vectors
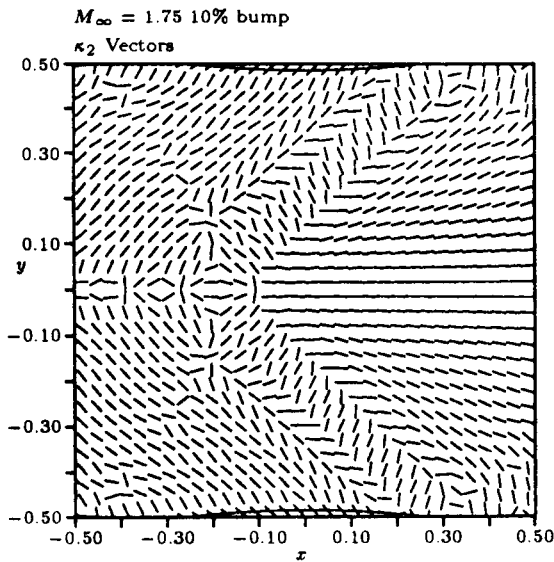
Figure 26: $M_\infty = 1.75$ Case — $\kappa^{(2)}$ Directions

$M_\infty = 1.75$ 10% bump
First Acoustic Convection
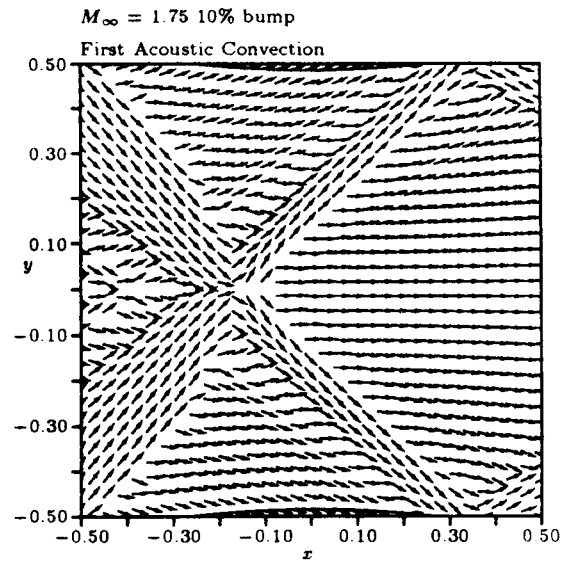
Figure 28: $M_\infty = 1.75$ Case — Convection Directions for First Acoustic-like Variable

14
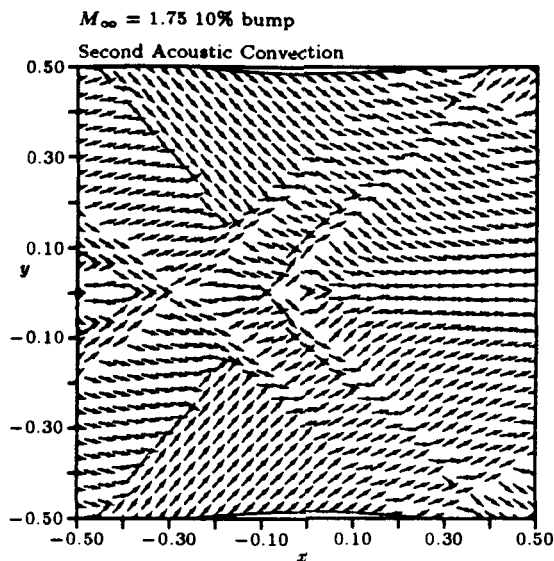
Figure 29: $M_\infty = 1.75$ Case — Convection Directions for Second Acoustic-like Variable

Figure 30: $M_\infty = 1.75$ Case — Effect of Local Δt (CFL=0.5)

Wave-preconditioning was also tried, but the lack of a precise control for the $\Delta t^{(k)}$ in regions where low wave speeds occur (inside steady shocks) made this calculation actually converge slightly more slowly than the calculation with spatial preconditioning only.

The results for the second case are shown in Figures 31–41. Figure 31 shows the Mach number contours for the steady flow. The shock pattern is similar to that of the first case, but the shocks move at a shallower angle, so that they do not reflect from the walls before reaching the outflow boundary. Due to the strength of the shocks in this case, some extra damping was necessary to capture them without large oscillations; this was provided by smoothing the residuals after each time-step with a biharmonic operator. Comparison results, non-limited and limited, are shown in Figures 32 and 33. Again, the new cell-vertex scheme gives virtually the same results as the non-limited cell-centered scheme. Figure 33 shows the substantial loss in resolution caused by turning on the limiter. The remaining plots again show the details of the shock-intersection region. Figure 34 shows the grid in this region; Figure 35 shows the Mach number contours. The $\kappa^{(1)}$ and $\kappa^{(2)}$ vectors are shown in Figures 36 and 37, the convection directions in Figures 38–40. Convergence histories for this case are shown in Figure 41. The three different convergence rates are for:

1. constant Δt (no preconditioning);

2. a different Δt in each cell (spatial preconditioning);

3. a different Δt for each convection equation (wave-preconditioning).

Due to the relatively high Mach number, the wave speeds do not exhibit much of a spread, so that the preconditioning gives only about a 20% gain. In this case, the convergence history clearly resembles that of the scalar equation: after 150 iterations, the residual drops rapidly.
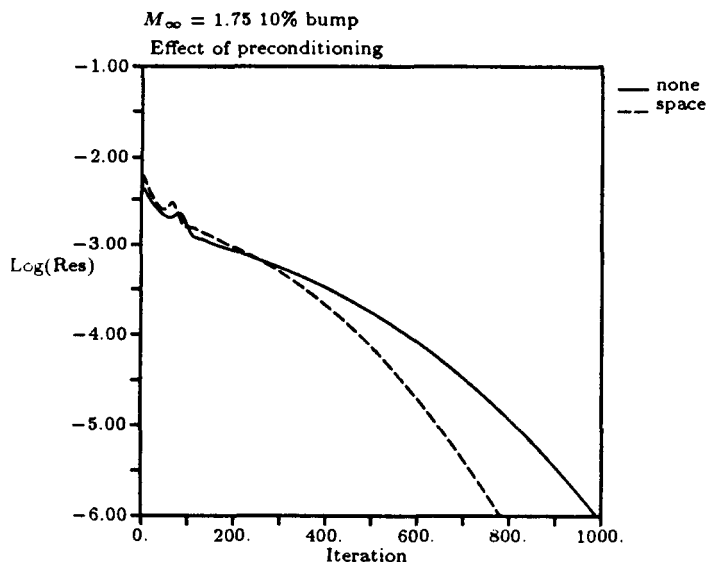
Conclusions

A genuinely multi-dimensional upwind-differencing cell-vertex scheme for a two-dimensional convection equation has been formulated, analyzed and tested. It has been extended to the Euler equations, giving a third-order accurate conservative scheme. The numerical results thus far are promising. The four essential elements of the Euler scheme are:
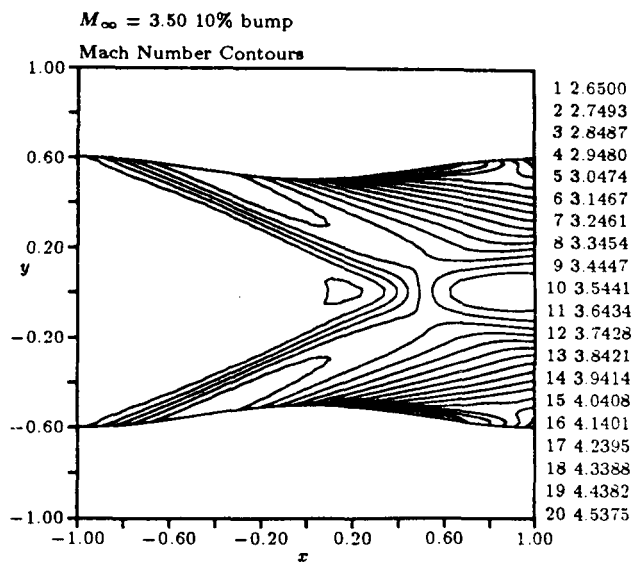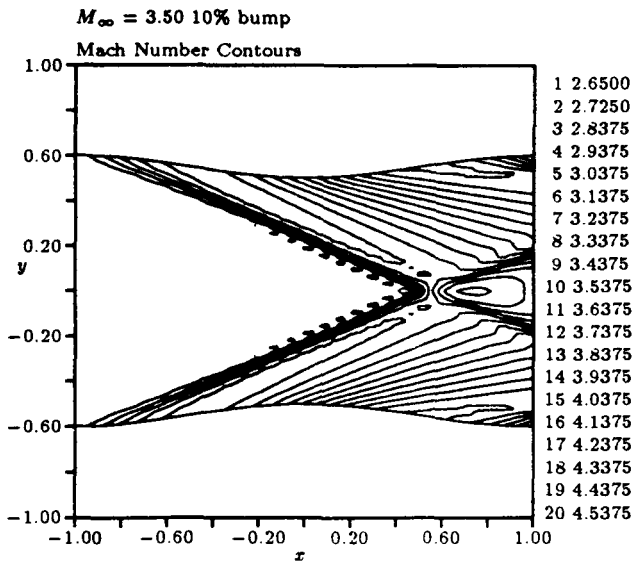
Figure 31: $M_\infty = 3.50$ Case — Mach Number Contours

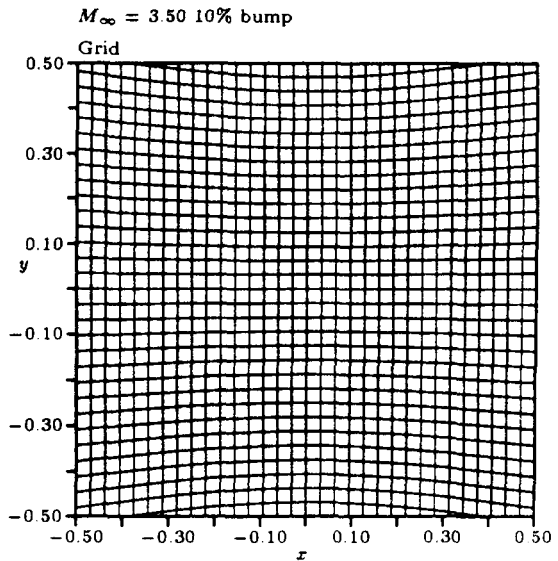Figure 33: $M_\infty = 3.50$ Case — Grid-Biased Upwind Results (Limiter On)
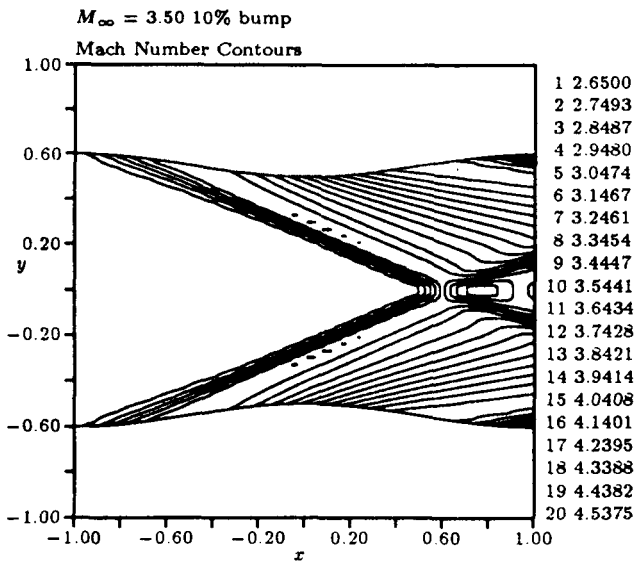

Figure 32: $M_\infty = 3.50$ Case — Grid-Biased Upwind Results (Limiter Off)

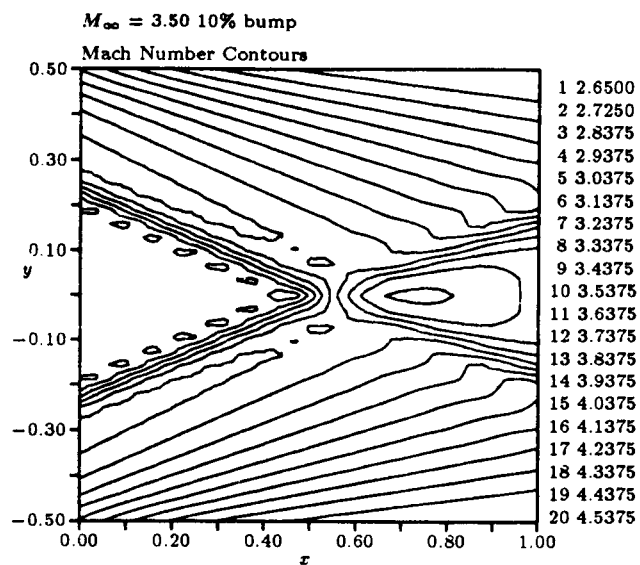Figure 34: $M_\infty = 3.50$ Case — Grid
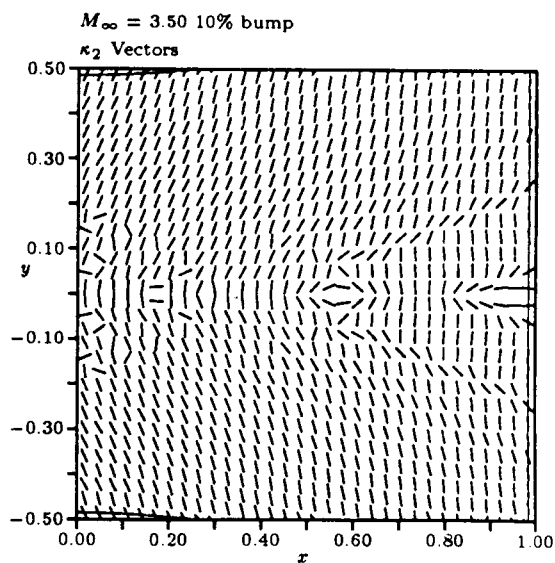
16

$M_\infty = 3.50$ 10% bump

Mach Number Contours

1	2.6500
2	2.7250
3	2.8375
4	2.9375
5	3.0375
6	3.1375
7	3.2375
8	3.3375
9	3.4375
10	3.5375
11	3.6375
12	3.7375
13	3.8375
14	3.9375
15	4.0375
16	4.1375
17	4.2375
18	4.3375
19	4.4375
20	4.5375

Figure 35: $M_\infty = 3.50$ Case — Mach Number Contours

$M_\infty = 3.50$ 10% bump

κ_2 Vectors

Figure 37: $M_\infty = 3.50$ Case — $\kappa^{(2)}$ Directions

$M_\infty = 3.50$ 10% bump

κ_1 Vectors
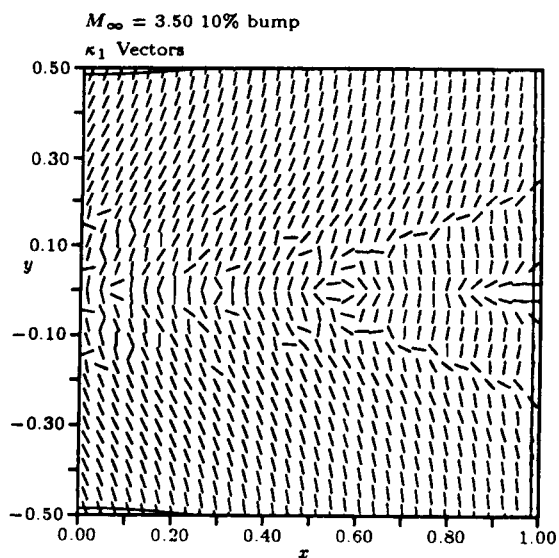
Figure 36: $M_\infty = 3.50$ Case — $\kappa^{(1)}$ Directions

$M_\infty = 3.50$ 10% bump

Entropy and Shear Convection
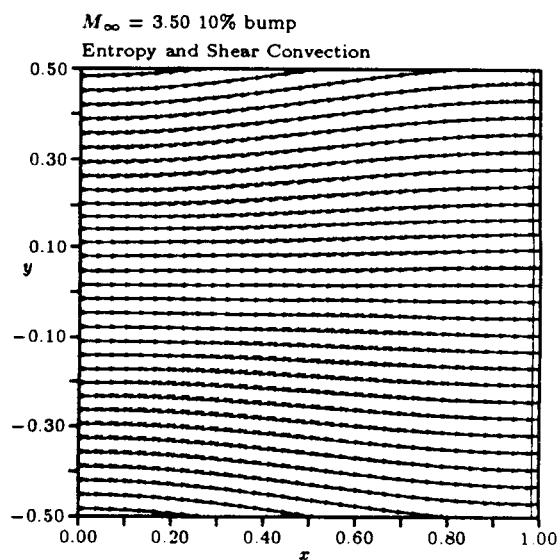
Figure 38: $M_\infty = 3.50$ Case — Convection Directions for Shear and Entropy

17
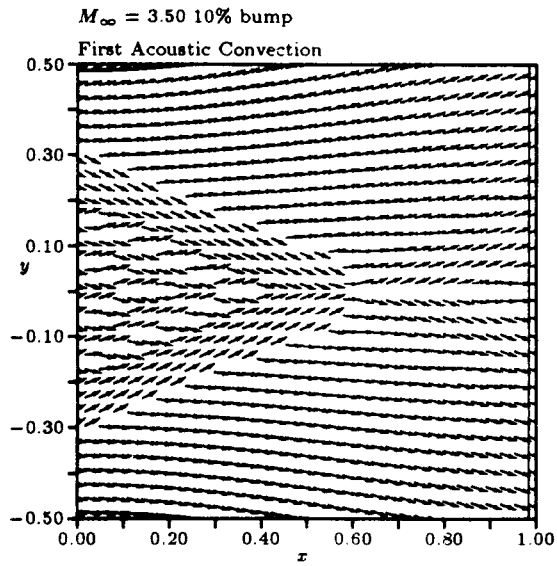
Figure 39: $M_\infty = 3.50$ Case — Convection Directions for First Acoustic-like Variable
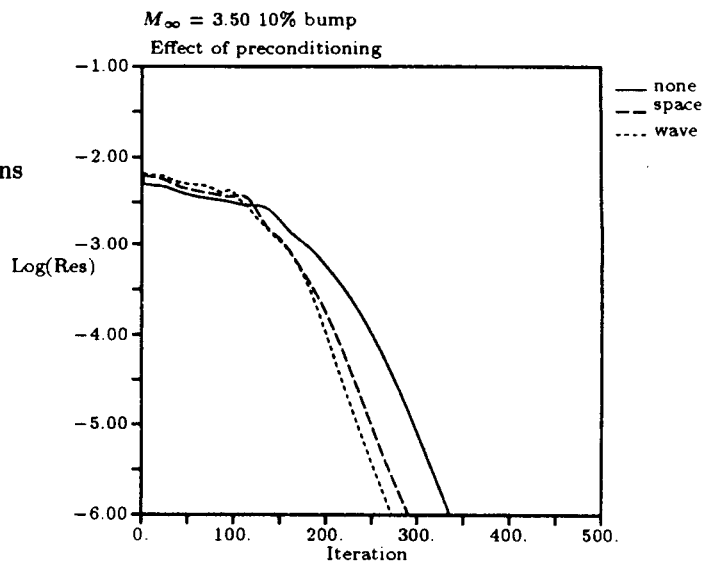
Figure 41: $M_\infty = 3.50$ Case — Effect of Local Δt and Characteristic Δt (CFL=0.5)
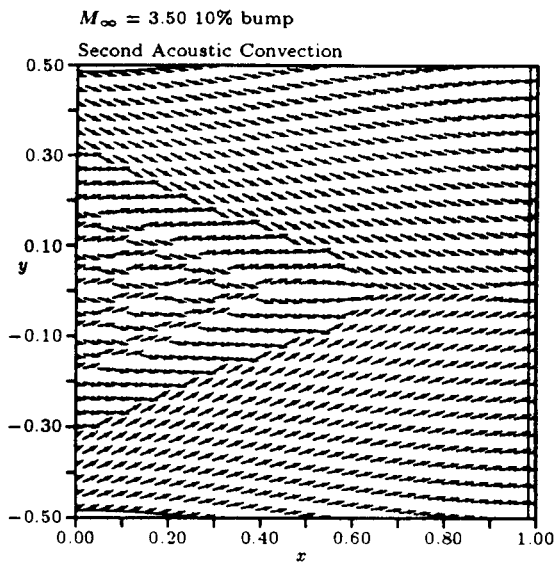
Figure 40: $M_\infty = 3.50$ Case — Convection Directions for Second Acoustic-like Variable

18

- the calculation of the convection directions;

- the residual calculation;

- the distribution step;

- the time-step calculation.

Three of the four warrant further study to produce a practical scheme.

The convection directions chosen here were the ones derived by Hirsch et al. [1]. As these are based on derivatives of the flow variables, the numerical values can be very noisy. One method used to minimize the effect of the noisiness of the Hirsch κ's was to freeze them after the residual had dropped two orders of magnitude. This improved convergence considerably. Experiments with other directions (e.g. the streamline direction) for the κ's showed that they *could* lead to faster convergence. Such alternative directions did not work in every case, however. Other wave models, such as that of Roe [2], remain to be investigated.

The residual calculation derived here gives third-order accuracy everywhere, which is not an advantage near shocks. It is not yet clear how to modify the residual formulas in order to ensure monotonicity. In addition, the highest-order terms in this scheme are strongly coupled to the choice of the κ's. These terms turned out to be destabilizing in regions where the κ's were highly oscillatory. In particular, subsonic cases (not shown here) converged only very slowly, and the final solutions were not smooth unless a more reliable fourth-order term (e.g. a biharmonic term) was added.

Not all of the underdamped behavior of the scheme can be traced to its high nonlinearity. As can be seen from Figure 10, the basic convection scheme does not damp any combination of a high spatial frequency along one coordinate with a low frequency along the other coordinate, if the convection is precisely in one of the coordinate directions. This lack of damping is caused by the vanishing of either θ_x or θ_y. Improvement of the convection scheme in this respect requres the introduction of additional finite-difference terms; these may actually be formulated as a smoothing term following the distribution step.

Finally, the time-step calculation, aimed at achieving optimal convergence, is far from robust. The technique of preconditioning by calculating a value of Δt for each convection equation, at each cell-vertex, can lead to large improvements in convergence [13,17]. When one of the convection speeds is very small, the potential benefit of wave-preconditioning is greatest, but so is the danger of taking the time step too large. A satisfactory analysis of this remains to be carried out.

Acknowledgments

References

[1] C. Hirsch, C. Lacor, and H. Deconinck, "Convection algorithm based on a diagonalization procedure for the multidimensional Euler equations," in *AIAA 8th Computational Fluid Dynamics Conference*, 1987.

[2] P. L. Roe, "Discrete models for the numerical analysis of time-dependent multidimensional gasdynamics," *Journal of Computational Physics*, vol. 63, 1986.

[3] G. Moretti, "The λ-scheme," *Computers and Fluids*, vol. 7, 1979.

[4] A. Verhoff and P. J. O'Neil, "A natural formulation for numerical solutions of the Euler equations," Tech. Rep. MCAIR 83-031, McDonnell Aircraft Company, 1983.

[5] S. F. Davis, "A rotationally-biased upwind difference scheme for the Euler equations," *Journal of Computational Physics*, vol. 56, 1984.

[6] D. Levy, K. G. Powell, and B. van Leer, "Implementation of a grid-independent upwind scheme for the Euler equations." Submitted for the AIAA 9th Computational Fluid Dynamics Conference, 1989.

[7] P. L. Roe, "Error estimates for cell-vertex solutions of the compressible Euler equations." ICASE Report 87-6, 1987.

[8] A. Jameson, "A vertex based multigrid algorithm for three-dimensional compressible flow calculations," 1986. Presented at the AME Symposium for Numerical Methods for Compressible Flow.

[9] K. G. Powell and E. M. Murman, "An embedded mesh procedure for leading-edge vortex flows," in *Proceedings of the Transonic Symposium*, 1988.

[10] M. G. Hall, "Cell-vertex multigrid schemes for so-
lution of the Euler equations," in *Numerical Meth-
ods for Fluid Dynamics II* (K. W. Morton and
M. J. Banes, eds.), Oxford University Press, 1986.

[11] R. H. Ni, "A multiple-grid scheme for solving the
Euler equations," *AIAA Journal*, vol. 20, 1981.

[12] P. L. Roe, "A basis for upwind differencing of
the two-dimensional unsteady Euler equations," in
Numerical Methods for Fluid Dynamics II, Oxford
University Press, 1986.

[13] B. van Leer, C. H. Tai, and K. G. Powell, "De-
sign of optimally-smoothing multi-stage schemes
for the Euler equations." Submitted for the AIAA
9th Computational Fluid Dynamics Conference,
1989.

[14] D. R. Lindquist and M. B. Giles, "A comparison
of numerical schemes on triangular and quadrilat-
eral meshes." Presented at the Eleventh Interna-
tional Conference on Numerical Methods in Fluid
Dynamics, 1988.

[15] P. W. Hemker and B. Koren, "Defect correction
and nonlinear multigrid for the steady Euler equa-
tions," Center for Mathematics and Computer Sci-
ence Note NM-N8801, Amsterdam, 1988.

[16] G. D. van Albada, B. van Leer,
and J. W. W. Roberts, "A comparative study of
computational methods in cosmic gas dynamics,"
Astronomy and Astrophysics, vol. 108, 1982.

[17] B. van Leer, W. T. Lee, and K. G. Powell, "Sonic-
point capturing." Submitted for the AIAA 9th
Computational Fluid Dynamics Conference, 1989.

Report Documentation Page

1. Report No. NASA TM-102029 ICOMP-89-13	2. Government Accession No.	3. Recipient's Catalog No.
4. Title and Subtitle A Genuinely Multi-Dimensional Upwind Cell-Vertex Scheme for the Euler Equations		**5. Report Date** May 1989
		6. Performing Organization Code
7. Author(s) Kenneth G. Powell and Bram van Leer		**8. Performing Organization Report No.** E-4772
		10. Work Unit No. 505-62-21
9. Performing Organization Name and Address National Aeronautics and Space Administration Lewis Research Center Cleveland, Ohio 44135-3191		**11. Contract or Grant No.**
		13. Type of Report and Period Covered Technical Memorandum
12. Sponsoring Agency Name and Address National Aeronautics and Space Administration Washington, D.C. 20546-0001		**14. Sponsoring Agency Code**

16. Abstract

A scheme for solving the two-dimensional Euler equations is developed. It is based on a new scheme for the two-dimensional linear convection equation, and the Euler-equation decomposition developed by Hirsch et al. [1]. The scheme is genuinely two-dimensional. At each iteration, the data are locally decomposed into four variables, allowing convection in appropriate directions. This is done via a cell-vertex scheme with a downwind-weighted distribution step. The scheme is conservative, and third-order accurate in space. The derivation and stability analysis of the scheme for the convection equation, and the derivation of the extension to the Euler equations are given. Preconditioning techniques based on local values of the convection speeds are discussed. The scheme for the Euler equations is applied to two channel-flow problems. It is shown to converge rapidly to a solution that agrees well with that of a third-order upwind solver.

17. Key Words (Suggested by Author(s)) Two-dimensional Euler equations Cell-vertex schemes Downwind weighting	18. Distribution Statement Unclassified – Unlimited Subject Category 64

19. Security Classif. (of this report) Unclassified	20. Security Classif. (of this page) Unclassified	21. No of pages 21	22. Price* A03